

Application of Organic and Copper-Oxide Superconductors for EPR Imaging

Yu. N. Shvachko¹, H.-H. Wang², and J. M. Williams²

¹Institute of Metal Physics, Russian Academy of Sciences, Ekaterinburg, Russian Federation

²Chemistry and Material Science Divisions, Argonne National Laboratory, Argonne, Illinois, USA

Received August 10, 2001; revised May 27, 2002

Abstract. A new electron paramagnetic resonance (EPR) imaging method on the surface of a superconducting finite-size plate is experimentally demonstrated. The single crystals of the layered organic charge-transfer salt $k\text{-(ET)}_2\text{Cu(NCS)}_2$ and copper oxide $\text{YBa}_2\text{Cu}_3\text{O}_{6.95}$ are applied to create field gradients up to 0.5 and 5 kG/cm respectively. Surface gradient mapping at different temperatures and dc field excursions is carried out. Qualitative explanation for the gradient mechanism in terms of the inhomogeneous critical state under field cycling is presented. Reconstruction of one-dimensional EPR images for model samples is presented at low temperatures. Spatial resolution of the order of 1 μm is experimentally reached on a standard X-band continuous-wave EPR spectrometer.

1 Introduction

Technical and methodological advances in nuclear magnetic resonance (NMR) tomography within the recent 20 years revolutionize its implementations from laboratory equipment into powerful commercial instruments for clinical diagnostics and a multifunctional tool for biological sciences and pharmaceutical industry. In comparison, modern advances of electron paramagnetic resonance (EPR) tomography are far less noticeable. The technical factors (gradients, sensitivity, time), which lie in the methodological peculiarities of EPR, still restrain the applications. Meanwhile, potential perspectives maintain a strong motivation for the search of new cost-effective solutions. The potential area for EPR imaging (EPRI) is expansive. Here are nondestructive testing of miniature composite samples, semiconducting, ceramic and polymeric films, membranes; heterogeneous catalysis; archeological dating and microdosimetry; mineralogy; tissue analysis and oxymetry; medical diagnostics, etc. [1–9]. As it was earlier emphasized [3], the combination of a portable EPR spectrometer with permanent magnet and an effective gradient device might lead to a significant step toward technological and biotechnological applications. EPRI is expected to be competitive at the “micron” spatial scale. We

believe that “EPR microscopy” (the term launched by M. Ikeya in 1990 [3]) is one of the most promising directions for the near future.

In order to obtain high-quality images, it is necessary to meet contradictory requirements for the hardware. On the one hand, the intensive gradients (much more intensive than those for nuclear magnetic resonance) are necessary for high resolution. For example, the 10 mm resolution in the objects where the EPR signal has the linewidth of 10 G (typical for radicals in many bioorganic substances) would require the creation of a 10 kG/cm gradient [10, 11]. It is technically difficult to reach such values by the external pair of coils or alternative electric devices. So far, the fruitful trend for the gradient enhancement has been focused on miniaturization of the devices and positioning them close to the sample inside the microwave (mw) cavity [3, 4]. However, the placement of conducting wires in the mw field leads inevitably to a drop of sensitivity. For a conventional continuous-wave (CW) X-band EPR spectrometer a “cross section” of 0.01 by 5 by 5 mm would be reliably detectable if the concentration of radicals is not less than 10^{15} cm⁻³. Taking into account the typical spin concentrations in bioorganic substances, the number of objects promising for EPR tomography diminishes drastically [2, 8]. To raise the sensitivity, on the other hand, one needs to increase the frequency moving to high-field EPR [14]. However, the design of modern high-field EPR spectrometers does not allow applications of already built devices for imaging. For the last 10 years, no considerable progress has been achieved in proposing new solutions for EPR tomography. This work is focused on a new approach to use bulk superconductors in the gradient devices.

The method presented in this work may be partially attributed to the “sensitive region methods” [1] where the gradient system (superconductor) is placed close to the sample inside the cavity. In earlier realizations, the anti-Helmholtz small coils [3, 4, 12, 13, 40], the ferromagnets [14–16], and the electromechanical devices [3, 12] have been already applied to produce the magnetic field gradient or move the local field domain over the studied surface. A new method is based on the following basic properties of anisotropic (layered) type II superconductors [17, 18].

1. In magnetic field B_0 ($B_{c1} < B_0 < B_{c2}$, where B_{c1} and B_{c2} are the lower and upper critical fields respectively), the superconductor is threaded by flux line (or Abrikosov vortices [23]) array, which produces the effective magnetization.

2. The sharp flux line concentration profile and very strong current are induced by the excursion (reversible change of the magnitude) of the external magnetic field (field excursion).

3. Flux lines can bend due to pinning anisotropy.

This work shows that by applying a field excursion procedure one can transform a superconducting substrate into a gradient device for magnetic resonance imaging. A sample under investigation is placed on the surface of a superconducting plate of length L between the center and the edge, $0 < z < L/2$, so that only one half of the surface is covered. The rest of the space, $-L/2 < z < 0$, can be used to monitor the gradient by reference probes. The highly conducting surface (ab) of the plate is aligned parallel to the external magnetic field B_0 and

is denoted as “lateral”. According to the isotropic pinning model [17–20], the field excursion creates a triangular distribution of flux-line density in the bulk of a superconductor. However, due to pinning anisotropy the extra flux does not leave the superconducting volume but is pushed onto the lateral surface. The cores of the flux lines produce an inhomogeneous local field. The spatial distribution of the local field on the lateral surface forms two symmetric segments along B_0 ($-L/2 < z < 0$, $0 < z < L/2$). Here the value of the gradient on the lateral surface is proportional to the critical current and the excursion magnitude. Thus, the problem of the gradient device is reduced to the manipulation with the flux tubes by building the peculiar (inhomogeneous) critical state. These aspects have not been discussed yet elsewhere.

2 Samples and Experimental Technique

2.1 Samples

The experiments were carried out on the superconducting single crystals k -(ET) $_2$ Cu(NCS) $_2$ [ET is bis(ethylenedithio)tetrathiafulvalene] with $T_c = 10.4$ K [21, 22] and YBa $_2$ Cu $_3$ O $_{6.95}$ with $T_c = 93$ K [23, 24]. Each sample, a plate of millimeter dimensions with thickness $D = 0.1$ – 0.3 mm, was mounted on a half-cylinder sample holder and/or a cylinder plastic plug on the bottom of the quartz tube (vertically or horizontally). Both compounds do not reveal an EPR signal below the superconducting temperature, T_c . It is known that a layered organic superconductor k -(ET) $_2$ Cu(NCS) $_2$ possesses the EPR line with $g_1 = 2.0095$ and $g_2 = 2.0057$, which undergoes dramatic broadening below the phase transition at $T = 36$ K. The temperature behavior of the EPR linewidth, ΔB , has been studied in ref. 25. Note that on approaching T_c the signal weakens and broadens, $\Delta B > 300$ G, and disappears below 10 K. Thus, at low-temperature measurements, $T < T_c$, this signal can be neglected. The EPR signal in stoichiometric YBa $_2$ Cu $_3$ O $_{6.95}$ was not found within the entire temperature range [24].

The highly conducting crystal face was set parallel to the external magnetic field, B_0 . Detailed field profiles on the surface were reconstructed with surface EPR probes. Thin needles (whiskers) and platelets of a recrystallized organic radical complex of α,γ -bis(diphenylene)- β -phenylallyl, BDPA, with benzene (1:1)

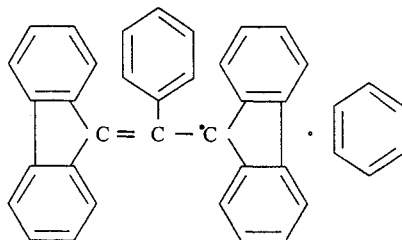


Fig. 1. BDPA free radical.

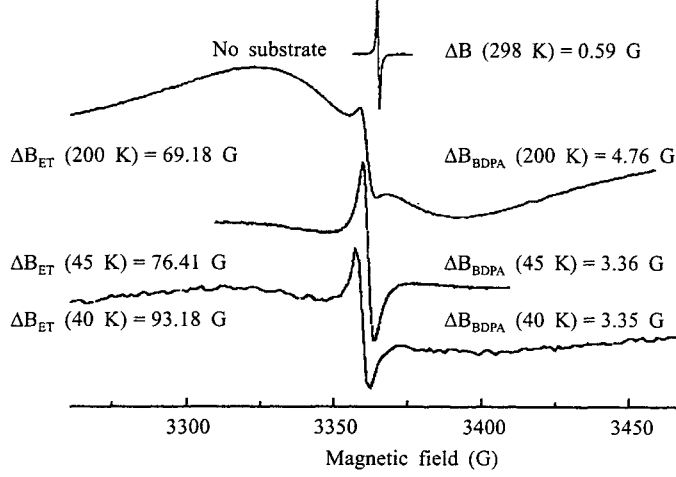


Fig. 2. EPR spectrum of BDPA fine particles (ΔB_{BDPA}) on the surface of $k\text{-(ET)}_2\text{Cu(NCS)}_2$ (ΔB_{ET}) at low temperatures. Broad ET signal disappears below the superconducting transition, $T < 11$ K.

were chosen as field-sensitive probes (Fig. 1). Typical dimensions were 200 by 100 by 5–10 μm and 200 by 10 by 10 μm , respectively. The BDPA radical possesses an intensive single EPR line, $\Delta B(298 \text{ K}) = 0.59 \text{ G}$, which gradually broadens at cooling, $\Delta B(4.2 \text{ K}) = 2\text{--}5 \text{ G}$, depending on the orientation of the microprobes. The temperature evolution of the EPR spectrum of the BDPA powder on the surface of $k\text{-(ET)}_2\text{Cu(NCS)}_2$ is shown in Fig. 2.

Parallel alignment of the plate in the field was set up by monitoring the hysteresis amplitude of nonresonance mw absorption [23, 26, 27]. The angular dependence of the mw hysteresis amplitude has a sharp peak at parallel configuration, which allows adjusting the orientation precisely [26–28]. Field-cooling procedure (cooling the sample in the magnetic field) with $B_0 = 3.36 \text{ kG}$ was applied down to $T = 4.2 \text{ K}$ for $k\text{-(ET)}_2\text{Cu(NCS)}_2$ and $T = 20, 40,$ and 60 K for $\text{YBa}_2\text{Cu}_3\text{O}_{6.95}$. These temperatures lie in the range of the irreversible behavior of the flux line array. Field sweep, δB_{sw} , necessary to record the EPR spectrum is $\delta B_{\text{sw}} \sim 5\Delta B_{\text{pp}}(T)$, where ΔB_{pp} is the peak-to-peak linewidth on the derivative curve, dP/dB . Typical values $5 \text{ G} < \delta B_{\text{sw}} < 100 \text{ G}$ did not exceed 10% of respective field excursion values. Therefore, the recording process does not dramatically perturb the flux-line distribution in the bulk.

2.2 Field Excursion Procedure

The field excursion procedure supposes increasing (decreasing) the amplitude of the external magnetic field up to (down to) a certain value $B_0 + B_{\text{up}}$ ($B_0 - B_{\text{down}}$). After that the field returns to its original value $B_0 = 3367 \text{ G}$, which is the resonance field for the EPR signal. For complicated spectra, B_0 has to be tuned to

the resonance field of the particular line under investigation. The procedure rate has to be within the limits of a quasistatic process and in our experiments is less than 500 G/min. The value B_{up} (B_{down}) is called the excursion field. A superconductor with the surface probes or the substance to study is cooled in the magnetic field B_0 down to temperatures $T < T_{\text{irr}} < T_c$ below the temperature of magnetic irreversibility, T_{irr} , which is detected by mw hysteresis. Figure 3 shows the evolution of the profiles for the critical current, $J_c(x)$, and the internal field density, $B_{\text{int}}(x) \sim \langle n\phi_0 \rangle_s$, $\phi_0 = hc/2e = 2.07 \cdot 10^{-7} \text{ G} \cdot \text{cm}^2$, in the bulk of a hard superconductor within the isotropic Bean model [17, 19, 20]. Here B_{int} is averaged

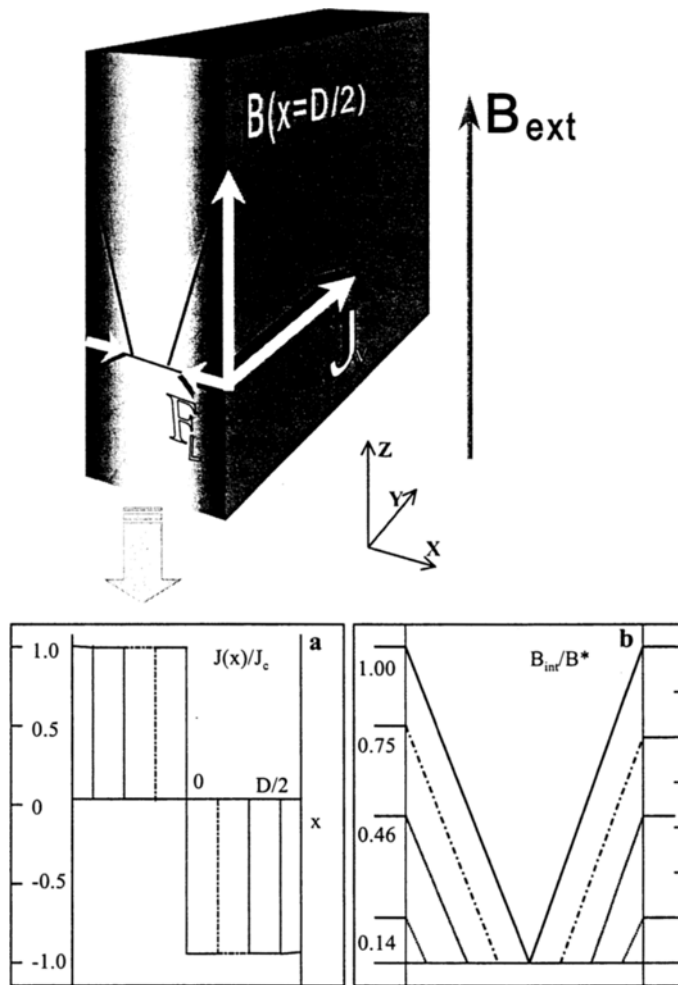


Fig. 3. Schematic diagram of the experimental geometry and the respective configuration of the internal field $B(x) = B_{\text{int}}(x) \sim \langle n\phi_0 \rangle_s$, critical current J_y , and Lorentz force F_L . The configuration corresponds to the isotropic Bean model (see text). **a** The bulk profile of the critical current density, $J(x)/J_c$. **b** The bulk profile of the internal field (magnetic flux density), B_{int}/B^* .

over the scale $S \gg d^2$, where d is the characteristic intervortex distance. The maximal value of B_{int} is limited by the critical value B^* . On returning to the original value B_0 , the inhomogeneous magnetic flux is trapped in the bulk. The extra flux lines leave the volume. Figure 4 shows the evolution of the frozen magnetic flux (internal gradient) at three different B_{up} values. Figure 4a demonstrates the internal profiles of flux-line density at different stages of the up-field excursion. Figure 4b shows the up-field excursion as the process developing in time (from top

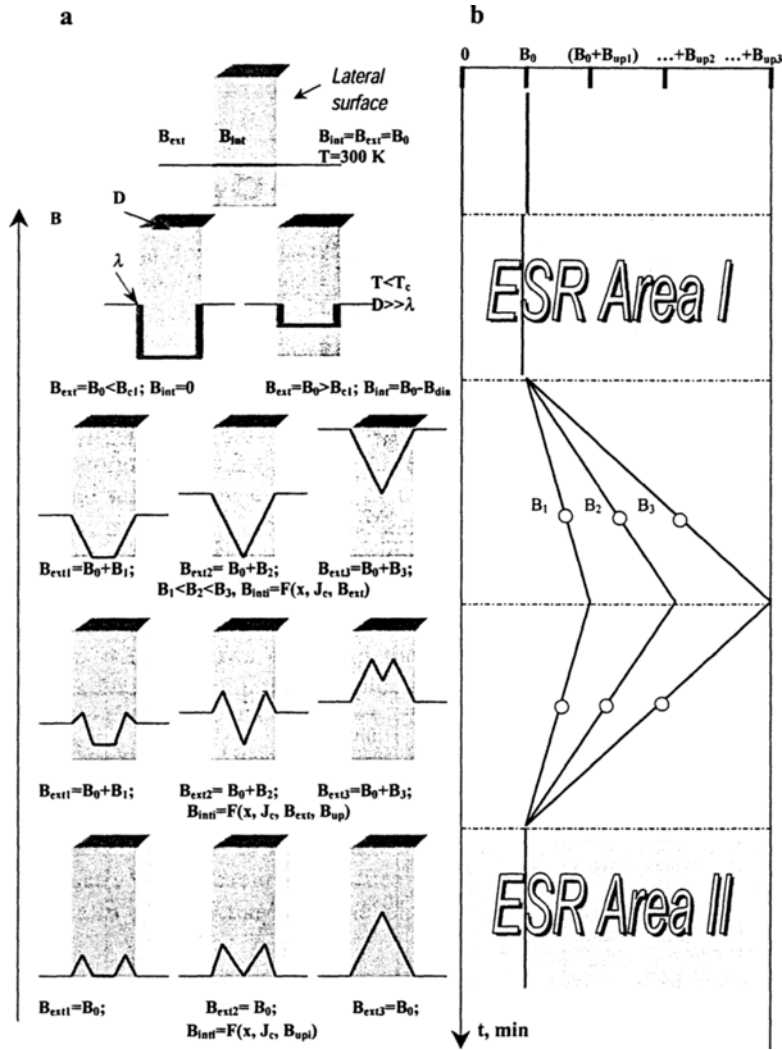


Fig. 4. Evolution of the bulk profile for the internal field at excursions with different B_{up} . Bulk profile is shown as a solid line on the cross section of the superconducting slab according to the configuration for B_{int}/B^* presented in Fig. 3. a Each row of slabs corresponds to the respective segment of "up-field" excursion in b. Three columns correspond to three different excursions (see text).

to bottom). Each row of slabs in Fig. 4a corresponds to the respective stage in Fig. 4b. The upper slab demonstrates homogeneous penetration of the external magnetic field into the bulk above T_c , $B_{\text{int}} = B_{\text{ext}}$. The lower row of slabs shows the internal field below T_c , where $B_{\text{ext}} = B_0 < B_{c1}$ and $B_{\text{ext}} = B_0 > B_{c1}$. Respectively, the internal field for the first case is $B_{\text{int}} = 0$, and for the second case $B_{\text{int}} = B_0 - B_{\text{dia}}$. In further consideration we neglect the London penetration depth, λ , because at fields and temperatures of the experiment the ratio $\lambda < d \ll D$ is always fulfilled. Besides, we do not take into consideration the Meissner fraction, B_{dia} , $B_{\text{int}} \approx B_0$ as soon as $B_0 \gg B_{c1}$ at studied ranges. Third and fourth rows of slabs reveal the internal profiles at increasing and decreasing stages of the field excursion depending on the B_{up} magnitude (see Fig. 4b). Three slabs at the bottom of Fig. 4a demonstrate the internal profiles after field excursions. The EPR probe deposited onto the lateral surface of the plate reveals the resonance signal before and after field excursion in areas denoted as ‘‘EPR Area I’’ and ‘‘EPR Area II’’ (Fig. 4b). The only difference of these two states is the trapped magnetic flux in the bulk of the superconducting substrate. It is found that the EPR signal in EPR Area II changes drastically compared to that in EPR Area I. The most reasonable explanation is the appearance of inhomogeneous local fields on the lateral surface. In this work we analyze the behavior of the EPR probe lineshape and resonance shift depending on the B_{up} values.

For a finite-size plate with thickness D there is a maximum field excursion value $B_{\text{up}}^* = 2B^*$, above which the profile and the value of the frozen flux remain unchanged. The value B_{up}^* is determined by the critical current density, i.e., by the concentration and character of pinning centers and temperature [18, 30]. For the critical profile within the Bean model, the value B_{up}^* , plate thickness, D , and critical current density, J_c , are connected by the relation [19, 20]

$$\frac{dB}{dx} = -\frac{4\pi}{c}J_c, \quad (1)$$

or

$$B_{\text{up}}^* = \frac{2\pi}{c}D \cdot J_c(T), \quad (2)$$

so that the value of the internal gradient is determined by the critical current (tangent of the angle at the basement of the triangular [critical] profile). It follows from Fig. 4 that after a sequence of N field cycles with the increasing excursion value, $B_{\text{up}}^1 < B_{\text{up}}^2 < B_{\text{up}}^3 < \dots < B_{\text{up}}^N$, the final profile of the magnetic flux (effective magnetization) will correspond to the last (largest) value of B_{up}^N . Thus, in one experiment (without heating above T_c) one can study the distributions of local fields at different B_{up} . As it is seen from Fig. 4a, the cases with $B_{\text{up}} < B_{\text{up}}^*/2$ can be considered as a sandwich, where two layers of the effective thickness h ($h < D$) with critical profiles are separated by the distance $(D - 2h)$. Hence, for the field probe on the lateral surface the change of field excursion would act like the manipulation with the thickness of the adjacent layer in which the critical profile of the magnetic flux (magnetization) is setting up.

2.3 Field Mapping

The teflon film with inserts of BDPA microprobes is mounted onto the lateral surface of a superconductor. The relative geometry and sizes of microprobes are determined with an optical microscope. For field mapping the needlelike BDPA microcrystals were mounted directly onto the surface with Apiezon vacuum grease. Before field excursions, all surface probes demonstrated a single EPR line, slightly shifted to lower fields relative to the signal of the isolated BDPA particle. This is well understood within the framework of the diamagnetic shielding (Meissner effect). With the EPR probe technique, the evolution of the flux-line condensate on the frontal surface (perpendicular configuration) of superconducting slabs has been studied earlier. For both macroscopic ($\gg d$) [31, 32] and microscopic ($\sim d$) [28, 29] scales the spatial concentration profiles and flux-line lattice parameters have been estimated. Unexpectedly, field excursion dramatically changes the EPR spectra of a spin probe on the lateral surface. Figure 5 shows schematically the typical EPR spectra of different surface probes after field excursion. The lineshapes observed in both organic and copper-oxide superconducting substrates have a similar behavior. Figure 6 shows the EPR spectrum of two spatially separated probes on the surface of a $k\text{-(ET)}_2\text{Cu(NCS)}_2$ single crystal, where $B_{\text{up}} = 6500$ G, $T = 4.2$ K. One can distinguish three effects of the same origin in the EPR spectrum: broadening, distortion, and splitting of the EPR signals (see Sect. 3.4). Owing to well-resolved splitting and distortions of individual lines and the known geometrical configuration of microprobes, it is easy to measure the amplitude of the local fields over small segments on the lateral surface (gradient mapping).

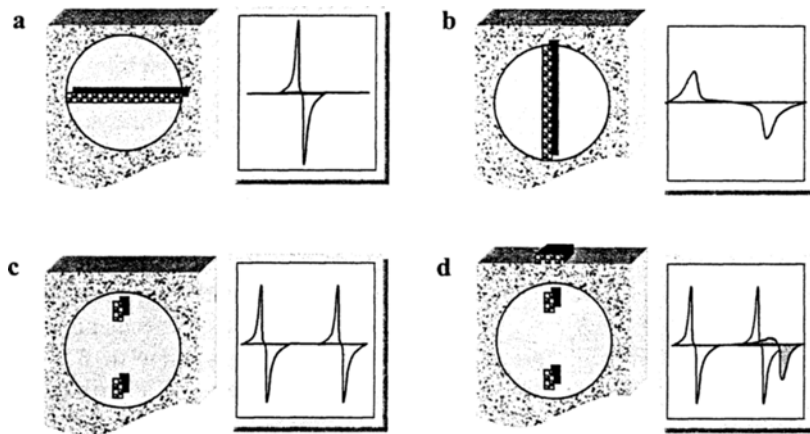


Fig. 5. Typical EPR spectra of the surface probes after field excursion. The BDPA whisker on the lateral surface is aligned perpendicular (a) and parallel (b) to the external field B ; c and d typical spectra for two and three microprobes. One of the probes (the BDPA platelet, d) is mounted on the frontal face of the crystal. Its asymmetric signal overlaps with the EPR spectrum of the probes on the lateral surface.

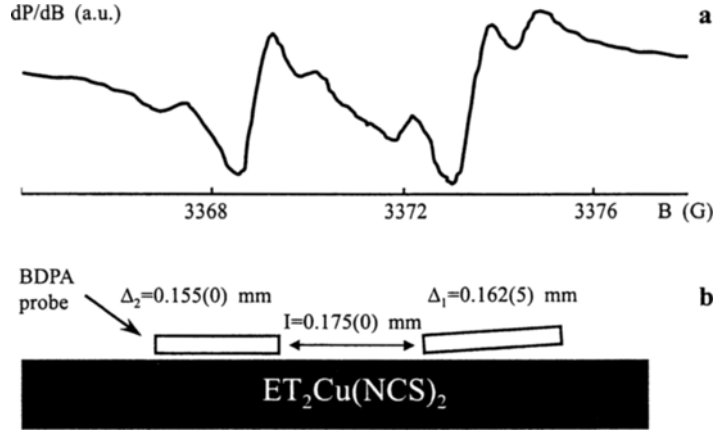


Fig. 6. **a** EPR spectrum (dP/dB) for two BDPA thin whiskers on the lateral surface of a k -(ET) $_2$ \times $Cu(NCS)_2$ single crystal after up-field excursion with $B_{up} = 6500$ G, $T = 4.2$ K. **b** The geometry of the experiment.

Gradient mapping was carried out with the following mutually consistent techniques.

1. From the inhomogeneous broadening of the EPR signal (for multiprobes, from the ratio of the broadening of a line attributed to an individual i -th probe, ΔB_i , to its length, $\Delta_i(z)$),

$$G_i(z) = \frac{\Delta B_i}{\Delta_i(z)}, \quad (3)$$

where $\Delta_i(z)$ is determined with the optical microscope.

2. From the field difference between EPR signals of individual probes:

$$G_{i-j} = \frac{B_{p-}^i - B_{p+}^j}{\Delta_j}, \quad (4)$$

where Δ_j is the distance between the i -th and j -th probes along the B_0 direction and B_{p-}^i and B_{p+}^j are the fields of the negative and positive peaks of the respective inhomogeneously distorted i -th and j -th lines.

3. By deconvolution of the EPR spectrum under the field gradient (for the single-platelet probes) [10, 11]:

$$h(B) = \int_0^{\infty} f(B - B')r(B')dB', \quad (5)$$

where the resulting spectrum, $h(B)$, is the convolution of an unperturbed signal $f(B - B')$ and the distribution function $r(B')$ characterizing the spatial distribu-

tion of the spin concentration. Formally, deconvolution is the integration of the Fourier transforms for extraction of the distribution function [33, 34]:

$$r(B) = \frac{1}{2\pi} \int_{-\infty}^{\infty} \frac{H(\omega)}{F(\omega)} \exp(i\omega B) d\omega, \quad (6)$$

$$H(\omega) = F(\omega)R(\omega), \quad (7)$$

where $H(\omega)$, $F(\omega)$, and $R(\omega)$ are the Fourier transforms of $h(B)$, $f(B)$, and $r(B)$ respectively. To simplify the procedure, the constant gradient G , which forms the spatial inhomogeneity $B(z) = B_0 + Gz$, was considered over the range $\Delta = (z_2 - z_1)$, corresponding to the probe size along the Z -axis. Then, the $r(B)$ function was reduced to

$$r(B) = \begin{cases} 0, & B < B_1 \\ \text{const}, & B_1 < B < B_2, \\ 0, & B > B_2 \end{cases} \quad (8)$$

where $B_1 = B(z_1)$ and $B_2 = B(z_2)$, so that $(B_2 - B_1)/\Delta = G$. Here the constant gradient and the homogeneous distribution of spins in the surface probe are suggested. Finally, the experimental single-probe spectra at different B_{up} values were simulated with G as a fitting parameter.

3 Results and Discussion

3.1 Field Distributions under Excursions

In Fig. 4 the up-field excursion is presented with the respective profiles of the internal field in the bulk of the superconducting substrate. Three cases, $B_{\text{up}} < B^*$, $B_{\text{up}} = B^*$, and $B_{\text{up}} = B_{\text{up}}^* = 2B^*$, are considered. At $T > T_c$ the field excursion does not influence the EPR parameters of the surface probe ($B_{\text{int}} = B_{\text{ext}}$). The respective EPR probe signal does not change compared to that of the isolated BDPA particle. After field cooling, $T < T_c$, the internal magnetic field as a sum of individual vortices distributes over the plate. For $B_{\text{ext}} > B_{\text{c1}}$, the flux lines spread homogeneously, so that $B_{\text{int}} = B_{\text{ext}} - B_{\text{dia}}$, where B_{dia} is the diamagnetic Meissner fraction [18, 23]. The upper B_{c1} estimates for $k\text{-(ET)}_2\text{Cu(NCS)}_2$ and $\text{YBa}_2\text{Cu}_3\text{O}_{6.95}$ are of the order of 10 and 500 G, respectively [24, 35]. For X-band EPR, $B_0 \sim 3300$ G, the relation $B_0 \gg B_{\text{c1}}$ is fulfilled for both compounds. At $B_0 \gg B_{\text{c1}}$, the diamagnetic shielding produces a minor effect, creating the redundant field in the vicinity of the lateral surface. This contribution proportional to the B_{dia} value is likely to be responsible for the negative shift of the resonance line in the EPR Area I. The observed shifts did not exceed $\Delta B_{\text{pp}}/2$. Hence, the EPR Area I corresponds to the substrate with the homogeneous internal field $B_{\text{int}}(x) \approx B_{\text{ext}} = B_0$ in the bulk.

During the field excursion the EPR signal cannot be detected because the external field is nonresonant. The up-field segment (third row of slabs in Fig. 4) creates the distributions similar to the profiles in Fig. 3. However, for $B_{\text{up3}} = 2B^*$ the “background” B_{int} value increases from about B_0 to $B_0 + B^*$. After the down-segment of the field excursion, the two symmetric sharp profiles of $B_{\text{int}}(x)$ are formed in the plate. Upon returning back, $B_{\text{ext}} \gg B_0$, two effective layers with a trianglelike distribution of the internal field (or effective magnetization via flux lines) set up. For $B^* < B_{\text{up}} < 2B^*$, the layers overlap. Thus, the critical state for the EPR Area II is characterized by the sharp spatial magnetization profile in the bulk. However, within the framework of the modified Bean theory for parallel alignment of superconducting plate [19, 20] there are no local fields on the lateral surface. Drastic changes of the EPR signal in the EPR Area II indicate the appearance of the inhomogeneous local field on the lateral surface. The question arises what the principal characteristics of this field are.

It was concluded from the experiments with various probes that the amplitude of the local magnetic field changes gradually along the $Z(B_0)$ -direction. Figure 5 shows schematically the typical spectra for different probes after the field excursion. Each panel in Fig. 5 consists of two parts. The left-hand part presents the shape, position and orientation of the probe on the superconducting plate. The respective EPR spectrum is presented in the right-hand part. The EPR spectrum in Fig. 5a enables one to conclude that the local field is uniform along the Y -direction. EPR spectra in Fig. 5b and c indicate that it changes gradually along the Z -direction. EPR spectra in Fig. 5c and d enable one to conclude that the magnitude of the local field on the lateral surface is related to the internal magnetic field (EPR signals in Fig. 5d overlap). Thus, the effect itself is not a boundary effect [18, 30] but the bulk effect resulting in the gradients on the lateral surface.

3.2 Organic Superconductor

The EPR spectrum for two probes on the surface of $k\text{-(ET)}_2\text{Cu(NCS)}_2$ presented in Fig. 6a corresponds to the situation in Fig. 5c. Figure 6a shows the experimental EPR spectrum after the up-field excursion. Figure 6b shows schematically the placement of the BDPA probes with their width and the interprobe distance. Note that only half of the superconducting substrate is shown, so that $0 < z < L/2$. The first experimental demonstration of the lineshape evolution for different surface probes has been presented in ref. 36. The satellite lines on the wings of the resolved signals relate to the geometrical edges of individual probes also shown in Fig. 5b. The ratio of the intensity of the central line and satellites varies for different individual probes. It may be reliably attributed to the nonideal shape of BDPA whiskers (platelets do not reveal central lines). Optical investigation confirms the nonideal shape of the whiskers. On the basis of the sizes of the probes, $\Delta_1 = 0.162(5)$, and $\Delta_2 = 0.155(0)$ mm, and the splitting between the respective satellite lines one can measure the gradient values $G = 21.30$ and 21.54

G/mm respectively. It is important to note that the gradient values at different points on the superconducting surface coincide. Despite reliable microscopic detection of the width, Δ (mm), the BDPA whiskerlike bars may not be ideally attached to the surface of the substrate (see the right-hand probe in Fig. 6b). By measuring the Z -coordinates of the probes one can easily reconstruct both local field values and the respective gradients over one half of the whole surface of the superconducting plate. For instance, the measurement of the distance between probes, $I = 0.175$ mm, gives the averaged gradient value over the space between probes $G = 18$ G/mm. This method is less reliable because of experimental difficulties to provide good configuration precision for BDPA whiskers to be parallel to the Y -direction.

The organic superconductors on the base of BEDT-TTF \equiv (ET) [22] are suitable objects to study the effects due to quasi-two-dimensional (2-D) anisotropy. The native pinning anisotropy is pronounced in k -(ET)₂Cu(NCS)₂ most effectively. There are some other experimental observations confirming the unusual critical state of layered organic superconductors [37]. However, the major drawback of organic superconductors is low critical currents, J_c [41]. From the qualitative consideration, the observed phenomenon is expected to be more pronounced in the anisotropic systems with stronger J_c values. The alternative promising choice for these studies might be the high- T_c systems, for instance, YBa₂Cu₃O_{6.95} single crystals.

3.3 Copper-Oxide Superconductor

The evolution of EPR spectra of BDPA probes on the YBa₂Cu₃O_{6.95} surface with up-field excursion is shown in Figs. 7 and 8 for single and double probes, respectively. It is evident that the increase of B_{up} leads to the gradient enhancement. The spectra in Fig. 7 are measured at $T = 20$ K and correspond to the thin single BDPA platelet. They are in good agreement with those in Fig. 5b. To demonstrate that the observed effects do not relate to a specific radical, an alternative experiment has been carried out. The spectra in Fig. 8 measured at $T = 20$ K originate from two microparticles of solid DPPH (diphenyl-picrylhydrazyl). The respective distortions and splitting are in good agreement with those in Fig. 5c. Similarly to the above procedure, by determining geometry and spacing between the probes one can easily calculate the gradient values and/or local field amplitudes at different points over the surface. The reverse is also true. From the gradient values one can reconstruct the spatial concentration profiles in the substances under investigation. For comparison, Fig. 9 shows EPR spectra at $T = 60$ K for the round spot of a DPPH radical (a model system). The drop of fine particle dispersion in ethyl alcohol has been extracted out of the upper (light violet in color) fraction. Then the spot of the diameter of 0.5 mm has been precipitated onto the thin teflon film and dried. The result shown in Fig. 9 can be considered as the 1-D spatial distribution of the spin concentration over the spot. The minimal concentration of the radical in the center of the

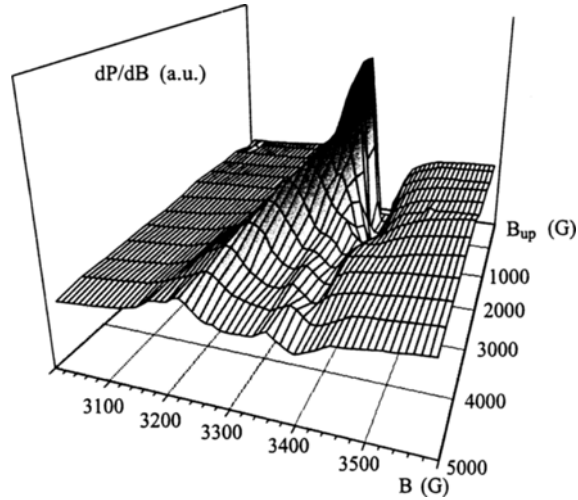


Fig. 7. Evolution of the EPR spectrum for a single BDPA platelet with increasing up-field excursion. The platelet is attached to the lateral surface of the $\text{YBa}_2\text{Cu}_3\text{O}_{6.95}$ single crystal. ΔB_{pp} (60 K) \approx 1 G at $B_{up} = 0$.

spot may indicate the motion of fine particles to the periphery during drying. This result looks realistic in terms of the interplay of the floating process and surface tension [43]. Note that this detected spatial distribution occurs on a micrometer scale.

Figures 10 and 11 show the result of the detailed 1-D gradient mapping at $T = 60$ K and different magnitudes of the up-field excursion. Note that only one

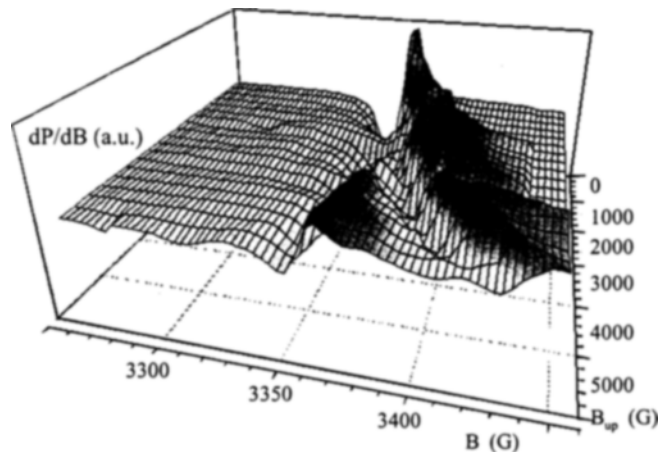


Fig. 8. Evolution of the EPR spectrum for two BDPA microprobes attached to the lateral surface of the $\text{YBa}_2\text{Cu}_3\text{O}_{6.95}$ single crystal. The splitting between signals does not saturate up to $B_{up} = 6500$ G reaching $\Delta B_{split} \approx 100$ G ($D = 0.130$ mm).

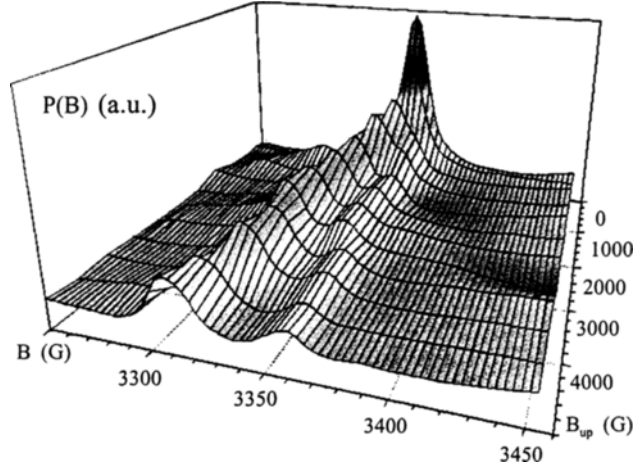


Fig. 9. Evolution of the absorption EPR signal for a DPPH spot deposited onto the thin teflon film. The film is mounted onto the lateral surface of the $\text{YBa}_2\text{Cu}_3\text{O}_{6.95}$ single crystal, ΔB_{pp} (60 K) \approx 3 G at $B_{up} = 0$. The spectrum with two maxima is the 1-D EPR image projection revealing the distribution of the radicals across the spot. The minimal amplitude in the center of the spectrum indicates the redistribution of the fine DPPH particles during drying.

half, $0 < z < L/2$, of the superconducting plate is shown on the top of Figs. 10 and 11. The mapping has been carried out by three BDPA whiskers aligned along the Y -direction. As a result, the analyzed spectra consist of three distorted EPR lines. The G_i and $G_{i,j}$ values are measured for each individual line and between lines (interprobe splitting) respectively. The dashed straight line is the result of deconvolution analysis. It follows from Fig. 10 that the measurements on individual lines G_i give the gradients approaching the value 300 G/mm within 15% at $B_{up} = 6500$ G. In Fig. 11 the same value measured by the interprobe method reaches 400 G/mm within 20%. Averaged measurements over the scale between first and third probes, depicted as G_{corr} , correlate with these estimates.

The discrepancy in the results of different measurement techniques can be explained by the influence of geometrical factors (similar to the case of organic superconductor). On the one hand, from measurements of the geometrical sizes of the probes the parameter D is attributed to the dimension of the whisker perpendicular to its main axis. On the other hand, by monitoring the angular dependence of the mw hysteresis amplitude the superconducting surface is oriented strictly parallel to the external field. When the above conditions hold, a small tilt (5–10°) of probes in the XY -plane may cause the effective “softening” of the borders due to nonorthogonality to B_0 . Consequently, the lineshape becomes more complicated and the respective G values are underestimated. Taking into account that similar trends are observed for each of three probes aligned parallel, one can assume that the small discrepancy is explained by the nonorthogonal contribution to the geometry of the experiment. For one of the probes ($i = 2$) the correction of the effective D size due to nonorthogonality

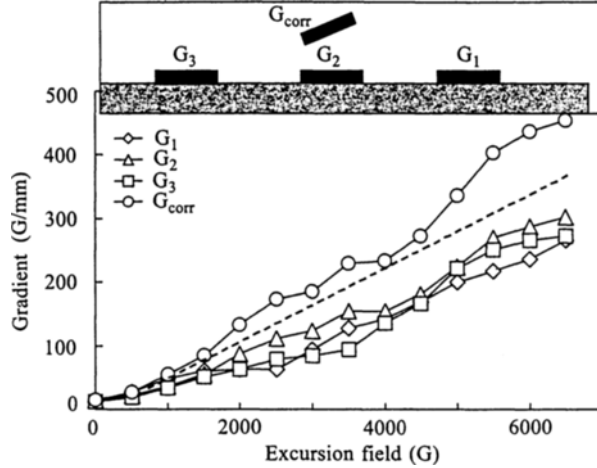


Fig. 10. Gradients G_i of the local field measured by three individual BDPA probes ($i = 1-3$) on the lateral surface of $\text{YBa}_2\text{Cu}_3\text{O}_{6.95}$ single crystal, $T = 60$ K. The G_i values are determined by the peak-to-peak linewidth for each of the resolved EPR lines. The schematic positions of the probes are presented on the top. The correction of the gradient, G_{corr} , is estimated for the nonparallel attachment of the BDPA platelet to the surface, where the angle is of the order of 30° . Dashed straight line is the result of the deconvolution of individual lines.

has been undertaken. The 30° misalignment has also been suggested for the estimate. Respective points depicted as G_{corr} in Fig. 10 are in good agreement with the series measured on interprobe scale and deconvolution results. It should be noted that scattering of the points in the range of $2000 \text{ G} < B_{\text{up}} < 4000 \text{ G}$ revealed in both Figs. 10 and 11 cannot be explained by the geometrical factor. It is likely due to the nonlinearity of the amplitude profile of the local field (for the above B_{up} interval), which is, in turn, caused by the peculiarity of the critical state.

The coincidence of G values measured at different points in the interval $0 < z < L/2$ (L – length of superconducting plate along B_0) and different field excursions, B_{up} , indicates linearity of the field amplitude profile along the Z -direction on one half of the lateral surface. The local field, $B_{\text{LF}}(z)$, on the other half of the lateral surface, $-L/2 < z < 0$, has the same amplitude and the opposite direction, $B_{\text{LF}}(z) = -B_{\text{LF}}(-z)$. In the performed experiments the ratio $D/L = 0.03-0.07 \ll 1$, hence this local field distribution cannot be explained by finite-size effects or demagnetization factors [18, 30]. It is found experimentally that the gradient, G , is proportional to the magnitude of field excursion, B_{up} . In the range of $0 \text{ G} < B_{\text{up}} < 3000 \text{ G}$ the ratio G/B_{up} is 0.06 mm^{-1} and within $4000 \text{ G} < B_{\text{up}} < 7000 \text{ G}$ it is 0.10 mm^{-1} respectively. This fact indicates that the magnetic flux on the one half of the lateral surface is proportional to the magnetic flux through the frontal surface. The total flux over the entire lateral surface is always zero. As the result of field excursion, the flux lines carrying the excessive flux do not leave the bulk of superconductor. Instead, they carry this flux

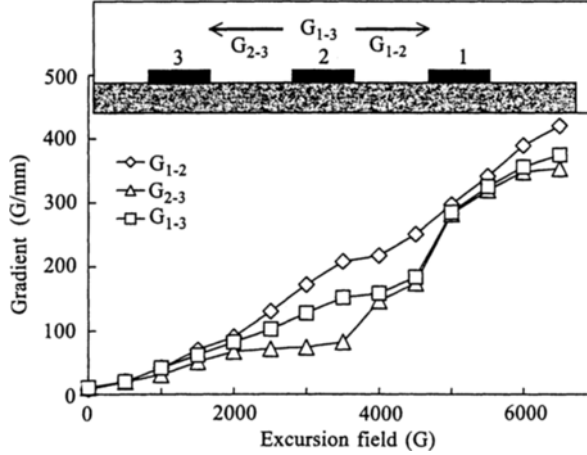


Fig. 11. Gradients, G_{ij} , of the local field obtained from the splitting of EPR lines for individual BDPA probes $i, j = 1-3$ on the lateral surface of $\text{YBa}_2\text{Cu}_3\text{O}_{6.95}$ single crystal, $T = 60$ K. The assignment is shown schematically in the above inset.

onto the lateral surface due to the bending effect. Each end of these extra vortex lines contributes to the respective segment of the local field density. Their distribution is symmetric with respect to the central plane of the crystal, $Z = 0$. Thus, the field excursion creates the inhomogeneous local field on the lateral surface. The 2-D pinning anisotropy stimulates this process and provides the mechanism for the topological transformation.

3.4 Critical State (Qualitative Explanation)

Figure 12 shows schematically the process of the magnetic flux penetration on the lateral surface. Figure 12a demonstrates the bent flux-line tails inside the superconducting plate near its edge. This boundary effect compensates the divergence of the local fields at the sharp boundary of the rectangular plate [18]. The flux-line cores in this small bent fraction produce the normal (in respect to the surface) component of the local field. Due to the quasi-2-D pinning anisotropy and interaction with critical current J_c , the tails of the flux lines carrying the normal component, F_0 , drift from the edge towards the center of the plate under the force $\mathbf{F} \sim [\Phi_0 \times \mathbf{J}_c]$. Thus, the vortex cores on the lateral surface move from the edge to the whole surface area. The motion stops when the “in-plane” pinning force compensates the driving force. As a result, the local field, $B_{\text{int}}(z)$, characterized by the normal component, covers the surface as it is shown in Fig. 12b. Flux flow takes place due to the lower “in-plane” pinning energy (read pinning force, $F_p \sim J_c B/c$) for the vortices drifting perpendicularly to highly conducting layers, F_p^\perp , i.e., $F_p^\perp \ll F_p^\parallel$. Finally, the drifting cores create the perpendicular component by pulling out the excessive flux onto the lateral surface.

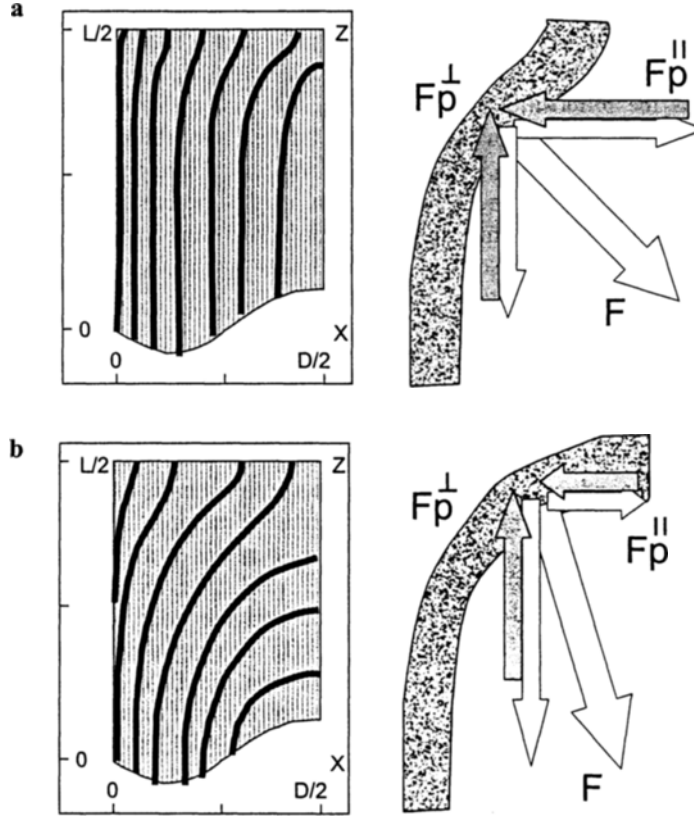


Fig. 12. Schematic diagram of the flux-line bending due to the boundary effect (a) and additional pinning anisotropy (b). For isotropic pinning, $F_p^{\perp} = F_p^{\parallel}$, the Lorentz force F is fully compensated unless in the vicinity of the edges. The strong 2-D pinning anisotropy, $F_p^{\perp} \ll F_p^{\parallel}$, causes the tangential component of the driving force F . Vortex lines move towards the crystal center until a new inhomogeneous critical state sets up ($J_c(x) \rightarrow J_c(x, z)$, $B_{int}(x) \rightarrow B_{int}(x, z)$).

Actually, the real picture is more complicated and further research is necessary to make it clear.

It is reasonable to suppose that the thermodynamically stable distribution of the magnetic flux on the lateral surface would also be characterized as a new effective critical state (similarly to the Bean approach), which as well produces linear gradients of local field density, $B_{int}(z) \sim Gz \perp B_0$. Note that in the perpendicular configuration the demagnetization factors lead to nonlinear field density profiles [20, 31, 32]. In our case the demagnetization factor does not contribute to the distribution on the lateral surface and the gradient is linear. Thus, the critical state in a layered superconductor transforms after field cycling into the nonuniform critical state, where all parameters of the model (B_{int} , J_c , etc.) depend on two coordinates, X and Z . At present, there is no theoretical model describing the

nonuniform critical state in anisotropic superconductors. Further analysis of the critical state lies beyond the subject of this work. Deeper insight and quantitative estimates will be given in a forthcoming paper. The practical consequence of our consideration is the proposition of the possible mechanism for creating the strong field gradients on the lateral surface. It also clarifies how these gradients can be governed by the field excursion. Note also that various technological methods exist which allow fabricating pinning anisotropy in hard superconductors. Heavy-ion irradiation, mechanical treatment, introducing defects during synthesis would substantially increase pinning anisotropy in traditional materials. Thus, the number of prospective materials expands.

3.5 Prototype Device for EPR

The opportunity to set up and control the local field distribution on the lateral surface of a superconducting plate allows one to consider it as a means to create a field gradient device for magnetic resonance imaging (MRI). In the simplest planar realization, the superconductor can work as a substrate for the object under investigation (film, plate, spots, etc.) [38]. The object covers half the area of the lateral surface between the middle and the edge, while the rest of space could be reserved for reference probes. On cooling down to the working temperature, the applied field excursion switches on the field gradient along the B_0 direction. In our experiments the local fields spread not exceeding $B_s^{\max} \sim 100$ G within the probe area, so that $B_s^{\max}/B_0 \ll 1$. Therefore, the deviation of the vector B from the Z -direction can be neglected. A step-by-step change of the “in-plane” angle φ between the characteristic axis of the studied object and the B_0 direction would give different “projections”, $h^\varphi(B)$. The 2-D MRI image of the object might be obtained from the standard procedure of reconstruction on projections $\{h^\varphi(B)\}$, for $0 < \varphi < 360^\circ$, which is well-known in EPR tomography (see Eqs. (6) and (7)) [6, 11, 33].

Figure 13 demonstrates the pilot realization of the above scheme. The plastic cylinder plug A is mounted on the bottom of the quartz tube B. A superconducting plate is inserted into the rectangular cleft fabricated on the top of the plug. The depth of the cleft is equal to the thickness of the plate. The plate is fixed horizontally on the top so that the tube axis divides the superconductor into the fragments of lengths $L/4$ and $3L/4$. The quartz rod with the plastic cylindrical head C is inserted into the tube. The head consists of two coaxial cylinders. The first cylinder with a diameter equal to the internal diameter of the tube provides the coaxial adjustment of the rod. The second cylinder on the bottom having a diameter of $L/2$ works as a sample holder. The top of the rod is connected to the goniometer, which allows rotation of the sample. Generally, the goniometer can be replaced by the stepmotor controlled by the computer. Then the recording procedure can be fully automated [42].

To demonstrate the advantages of the new technique, we reconstruct the 1-D distribution of the radical in the model sample. The scheme of the experiment is

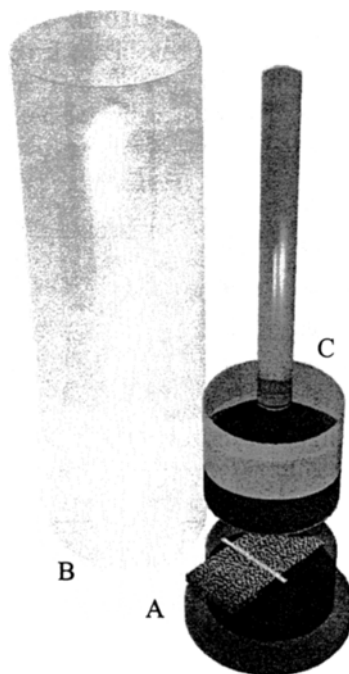


Fig. 13. Gradient device for EPR imaging: A, a plastic plug with the superconducting plate inserted into the cleft on its surface; B, a quartz tube; C, a quartz rod with the coaxial cylinder head and sample holder.

shown in Fig. 14a, where the sample, a disk with radicals D, is attached to the surface of superconductor A. The model radical system, a dispersion of BDPA fine particles in ethyl alcohol, is a series of individual drops deposited onto a disk of filter paper and dried out. The position and size of every spot is determined with an optical microscope. Schematically they are shown enlarged in D. On cooling below T_c , the intensive symmetric EPR signal has been detected. On application of the up-field excursion, $B_{up} = 6000$ G, the signal dramatically change into series of distorted lines. Rotating the sample we observe a set of different EPR spectra. These spectra are interpreted as a 1-D projection of the spatial radical distributions along the direction of the external magnetic field. The scale of distribution is determined by the external field gradient (i.e., B_{up}). One of the 1-D-projections is shown in Fig. 14b as the resolved EPR derivative spectrum, dP/dB , and as the absorption signal, $P(B)$ (first integral of dP/dB). By using the original BDPA lineshape and simple deconvolution procedure we obtain the distribution of the radical along the chosen direction. The sketch on the bottom (Fig. 14c) is the 1-D reconstruction of the spatial BDPA concentration profile. A comparison of the model sample with the BDPA spots D and 1-D image reconstruction (Fig. 14c) gives satisfactory agreement. Note that in contrast to the distribution in Fig. 8 (teflon substrate), the radical concentration in the centers of in-

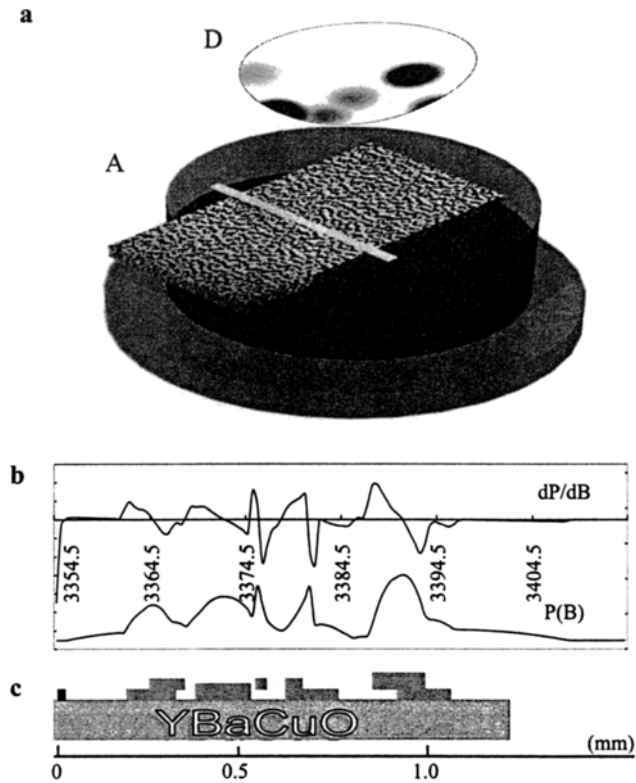


Fig. 14. **a** Scheme of the EPRI experiment: A, enlarged view of the plug and the model film D under investigation. The positions of the BDPA radical centers detected with an optical microscope are shown schematically as the dark spots. **b** The EPR spectrum, dP/dB , and its first integral, $P(B)$. **c** The qualitative reconstruction of the concentration profile.

dividual spots is maximal. We conclude that the particle distribution in the individual spot is determined by the substrate.

We believe that the experimental data and the concept demonstrate the consistent arguments in favor of the new superconducting gradient device for magnetic resonance imaging. The potential applications are not limited to continuous-wave EPR. For the pulsed EPR and NMR techniques and high-field EPR, in particular, there must be new advantages due to the measurements in the static magnetic field.

3.6 Comparison with Existing Solutions

To emphasize the advantages we present the estimates for spatial resolution of the superconducting gradient device in our experiments. The data demonstrated in Figs. 10 and 11 prove the spatial resolution of the order of about 1 μm . In-

deed, as for the probe size of 0.05 mm (whisker) on the $\text{YBa}_2\text{Cu}_3\text{O}_{6.95}$ surface ($T = 60$ K, $B_{\text{up}} = 6.5$ kG) the achieved broadening is about 30 G, then the strip of 1 mm would give the linewidth of about 0.6 G. The linewidth of the fine BDPA particle at these temperatures is close to 0.6 G. Therefore, the splitting of the EPR signal for two probes at the 1 μm distance is of the order of the native BDPA linewidth, which is reliably detectable, provided the sensitivity is high enough.

It should be noted that the achieved high gradients are not limited by the physical properties of studied materials. No special efforts were made to influence the concentration of pinning centers (ion-beam irradiation, deformation, etc.), geometrical sizes of superconducting substrates, or to build the composite devices with the aim of further gradient enhancement. It is likely that the optimized values may be of the order of magnitude higher. However, these aspects in greater perspective deal with the advanced engineering solutions and can be the subject of separate studies. To estimate the effectiveness of the new approach, it is reasonable to compare the parameters of existing gradient devices for EPR.

For example, the miniature pair of anti-Helmholtz coils with a diameter of 0.5–2 mm (from 3 to 20 turns) and a gap size of 1–3 mm allows to reach gradients of up to 200 G/mm at $I = 5$ A. The gradient system is placed close to the sample inside the mw cavity [1]. The main drawbacks of this approach are the microwave losses caused by the insertion of the coils and heating. Replacement of the mw cavity by an ensemble of mw coils allows to reach gradient of 330 G/mm within the range of 10 mm diameter (90 turns of anti-Helmholtz system, $I = 30$ A) [13]. The cross section of the sample must not exceed 0.2 mm and a special cooling jacket is required to maintain thermal stability. The “8-shaped” coils allow to create gradients along the X - and Y -directions. The values for this design could reach $G = 500$ G/cm at $I = 4$ A. The authors estimate the maximum values for similar devices as 2 kG/cm [3]. Note that for low-temperature studies all mentioned realizations are practically hopeless. The alternative approach on the basis of the application of ferromagnetic attachments has been developed by Lebedev et al. [14, 15, 25]. In contrast to a superconductor, the application of a ferromagnet in EPR experiments strongly perturbs the external magnetic field due to the extremely high magnetic susceptibility of these materials and demagnetization effects. High-field EPR is more preferable for such a gradient system because the ferromagnetic inclusions (disks, wedges) can be attached to the outer part of the mw cavity. However, the obtained gradients are not uniform throughout the sample and the reconstruction of the spatial distribution is complicated [14].

The alternative ideology of the electromechanical approach is based on mechanical scanning of the pinhole modulation region (scanning EPR microscopy via a modulation coil), active domain on the orthogonal arrays of microfabricated network (wires switch the local field domains), and/or focused microwaves (scanning via a pinhole mw region). Respective devices are usually the state-of-art units, which cannot be compared by their physical principles and easily reproduced commercially [2, 3]. However, the common disadvantages are heating (high

current leads to heating of thin wires) and low sensitivity (additional objects in a resonator suppress the Q -factor).

Ikea et al. [3] proposed that the usage of superconducting wires in the “8-shaped” scheme would rise the gradient values up to 20 kG/cm at $T = 4$ K. However, this proposal has not been fulfilled so far. We believe that the approach presented in our work allows to reach this limit. Thus, the inhomogeneous critical state in anisotropic superconductors gives the alternative physical basis for the development of competitive cost-effective solutions for EPR imaging and microscopy.

4 Summary

This work proposes and demonstrates experimentally a new solution for EPRI at low temperatures. The method allows to study the EPR centers in thin films at low temperatures without modification of the routine experimental equipment. It is shown that the strong superconducting current and flux-line distribution induce linear field profiles on the lateral surface of a superconductor. The gradient values of $G = 0.5$ and 5.0 kG/cm are experimentally achieved. However, for further development a deeper insight into the peculiarities of the critical state is required. Qualitative consideration presented in the work fails to explain the increase of the gradient values with the excursion field. Direct expansion of the isotropic Bean model into the 2-D case does not work properly. A quantitative model linking pinning anisotropy and rearrangement of the flux-line array under the field cycling has to shed light onto the mechanisms of the gradient formation. A detailed experimental investigation of the inhomogeneous critical state by the EPR probe decoration will be published in a forthcoming paper. Alternative experiments (field-sensitive STM, optics, etc.) for the direct observation of the vortex cores on the lateral surface would be very helpful.

The basic principles shown in this work open the ample opportunities for new engineering realizations. In particular, the preparation of a sandwich superconductor-sample-superconductor is expected to double the gradient and spatial resolution. The combination of several superconducting elements may lead to orthogonal gradient systems. The prototype device for 2-D imaging described in this work allows the application of heliconlike recording where each step in field sweep is associated with full rotation of the sample. Finally, within one field sweep the matrix of $P(j_i, B_j)$ can be extracted [39]. The series of projections $h^n(B)$ necessary for image reconstruction would be the cross sections of the surface $P(j_i, B_j)$ which fit the matrix data.

Acknowledgements

This work was supported by the Russian Foundation for Basic Research (RFBR) under grants nr. 96-04-19427 and nr. 00-15-96745. The chemical part of the work

and experiments at Argonne National Laboratory (Argonne, USA) have been supported by NATO under Linkage Grant nr. SA.12-3-02 (HTECH.LG950108) 655(95) JARC412 (Yu.N.Sh. and H.-H.W.). The preparation of this work in its final form was supported in part by the Netherlands Organization for Scientific Research (NWO) under Contract nr. 047.008.020 (Yu.N.Sh.). We are also thankful to Dr. U. Welp for providing YBaCuO single crystals and to Dr. J. Schlueter for helpful participation.

References

1. Lebedev Ya.S. in: *Modern Pulsed and Continuous-Wave Electron Spin Resonance* (Kevan L., Bowman M.K., eds.), p. 365. New York: Wiley 1990.
2. Eaton G.R., Eaton S.S., Ohno K. (eds.): *EPR Imaginig and In Vivo EPR*. Boca Raton, Fla.: CRC Press 1991.
3. Ikeya M., Furusawa M., Ishii H., Miki T.: *Appl. Magn. Reson.* **1**, 70 (1990)
4. Ikeya M.: *Appl. Magn. Reson.* **1**, 14 (1991)
5. Woods R.K., Basic G.C., Lautherbur P.C., Swartz H.M.: *J. Magn. Reson. B* **84**, 247 (1989)
6. Yakimchenko O.Ye., Smirnov A.I., Lebedev Ya.S.: *Appl. Magn. Reson.* **1**, 1 (1990)
7. Kuppusamy P., Chzan M., Zweier J.: *J. Magn. Reson. B* **106**, 122 (1995)
8. Berliner L.J., Fuji H.: *Magnetic Resonance in Biology and Medicine*. New Delhi: Tata McGraw-Hill 1985.
9. Berliner L.J., Fuji H., Wan X., Lukiewicz S.J.: *Magn. Reson. Med.* **4**, 380 (1987)
10. Wendsrdorfer E., Karthe W.: *J. Magn. Reson.* **33**, 107 (1979)
11. Herrling Th., Klimes N., Karthe W., Ewert U., Ebert B.: *J. Magn. Reson.* **49**, 203 (1982)
12. Ikeya M., Miki T.: *Jpn. J. Appl. Phys.* **26**, L929 (1987)
13. Ohno K., Murakami T.: *J. Magn. Reson.* **79**, 343 (1988)
14. Smirnov A.I., Poluectov O.G., Lebedev Ya.S.: *J. Magn. Reson.* **97**, 1–12 (1992)
15. Yakimchenko O.Ye., Lebedev Ya.S.: *Khim. Fiz.* **3**, 641 (1984)
16. Smirnov A.I., Degtyarev E.N., Yakimchenko O.Ye., Lebedev Ya.S.: *Prib. Tekh. Eksp.* **2**, 100 (1988)
17. Bean C.P.: *Rev. Mod. Phys.* **36**, 31 (1964)
18. Campbell A.M., Evetts J.E.: *Critical Currents in Superconductors*. London: Taylor and Francis 1972.
19. Brandt E.H., Indenbom M.: *Phys. Rev. B* **48**, 12893 (1993)
20. Zeldov E., Clem J.R., McElfresh M., Darwin M.: *Phys. Rev. B* **49**, 9802 (1994)
21. Saito G., Urayama H., Yamochi H., Oshima K.: *Synth. Met.* **27**, A331 (1988)
22. Williams J.M., Ferraro J.R., Thorn R.J., Carlson K.D., Geiser U., Wang H.H., Kini A.M., Whangbo M.-H.: *Organic Superconductors (Including Fullerenes): Synthesis, Structure, Properties, and Theory*. Englewood Cliffs, NJ: Prentice Hall 1992.
23. Portis A.M.: *Electrodynamics of High-Temperature Superconductors, Lecture Notes in Physics*, vol. 48. Singapore: World Scientific Publishing 1993.
24. Romanyukha A.A., Shvachko Yu.N., Ustinov V.V.: *Usp. Fiz. Nauk* **161**, 37 (1991)
25. Romanyukha A.A., Shvachko Yu.N., Skripov A.V., Ustinov V.V.: *Phys. Status Solidi B* **151**, K59 (1989)
26. Shvachko Yu.N., Khusainov D.Z., Romanyukha A.A., Ustinov V.V.: *Solid State Commun.* **69**, 611 (1989)
27. Romanyukha A.A., Khusainov D.Z., Shvachko Yu.N., Koshta A.A., Ustinov V.V.: *Phys. Met. Metallorg.* **80**, 142 (1995)
28. Shvachko Yu.N., Koshta A.A., Romanyukha A.A., Naumov S.V., Ustinov V.V.: *Physica C* **197**, 27 (1992)
29. Shvachko Yu.N., Koshta A.A., Romanyukha A.A., Ustinov V.V., Akimov A.I.: *Physica C* **174**, 447 (1991)
30. Gurevich A.V., Mints R.G., Rahmanov A.L.: *Physics of Composite Superconductors*. Moscow: Nauka 1987.

31. Khasanov R.I., Talanov Yu.I., Vashakidze Yu.M., Teitel'baum G.B.: *Physica C* **235–240**, 2935 (1994)
32. Khasanov R.I., Talanov Yu.I., Assmus W., Teitel'baum G.B.: *Phys. Rev. B* **54**, 13337 (1996)
33. Herman G.T.: *Image Reconstruction from Projections*. New York: Academic Press 1980.
34. Herman G.T., Natterer F. (eds.): *Mathematical Aspects of Computerized Tomography*, vol. 8, p. 225. Berlin: Springer 1981.
35. Kwok W.K., Welp U., Paulius L.M., Vinokur V.M., Petrean A.M., Ronningen R.M., Crabtree G.W.: *Phys. Rev. B* **42**, 8686 (1990)
36. Shvachko Yu.N., Wang H.-H., Williams J.M. in: *Proceedings of the Joint 29th AMPERE and 13th ISMAR International Conference*, p. 1107. August 2–7. Berlin 1998.
37. Lahaise U.G., Qun Chen, De Long L.E., Brock C.P., Wang H.H., Carlson K.D., Schlueter J.A., Williams J.M.: *Phys. Rev. B* **51**, 3301 (1995)
38. Shvachko Yu.N., Wang H.-H., Williams J.M. in: *Proceedings of the Joint 29th AMPERE and 13th ISMAR International Conference*, p. 214. August 2–7. Berlin 1998.
39. Shvachko Yu.N., Starichenko D.V., Shmatov G.A., Gobov Yu.L.: *Phys. Solid State* **44**, 2124–2129 (2002)
40. Sueki M., Eaton G.R., Eaton S.S.: *Appl. Magn. Reson.* **1**, 20 (1990)
41. Gonzalez M.A., Velez M., Vincent J.L., Schlueter J., Williams J.M., Crabtree G.W.: *Physica C* **235–240**, 2471 (1994)
42. Shvachko Yu.N., Wang H.-H., Williams J.M. in: *Proceedings of the International Workshop “Modern Development of Magnetic Resonance Imaging and Spectroscopy. Basic Physics and Applications in Medicine and Biology”* (Aganov A., Il'yasov A., eds.), June 11–13, 2001. Kazan.
43. Deegan R.D., Bakajin O., Dupont T.F., Huber G., Nagel S.R., Witten T.A.: *Nature* **389**, 827 (1997)

Authors' address: Yuri N. Shvachko, Institute of Metal Physics, Russian Academy of Sciences, Ulitsa S. Kovalevskoi 18, 620219 Ekaterinburg, Russian Federation